Optics and Lasers in Engineering 172 (2024) 107882

Contents lists available at ScienceDirect

Optics and Lasers in Engineering

journal homepage: www.elsevier.com/locate/optlaseng

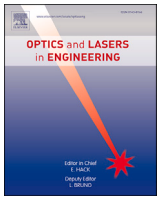

Collimated phase measuring deflectometry

Lei Huang [a,*], Tianyi Wang [a], Corey Austin [a], Lukas Lienhard [a], Yan Hu [b], Chao Zuo [b], Daewook Kim [c], Mourad Idir [a]

[a] National Synchrotron Light Source II (NSLS-II), Brookhaven National Laboratory, PO Box 5000, Upton, NY 11973, USA
[b] Smart Computational Imaging Laboratory (SCILab), School of Electronic and Optical Engineering, Nanjing University of Science and Technology, Nanjing, Jiangsu 210094, China
[c] Large Optics Fabrication and Testing Group, Wyant College of Optical Sciences, University of Arizona, 1630 E. University Blvd., Tucson, AZ 85721, USA

ABSTRACT

Phase measuring deflectometry has been applied for free-form specular surface metrology, but its measured slope results are sensitive to the depth of sample positioning, which is also called the height-slope ambiguity. The objective of this work is to tackle this height-slope ambiguity problem. The main idea is to introduce collimated camera rays using a telecentric imaging lens and collimated structured-light illumination with a Fourier lens. This setup makes the fringe phases become only sensitive to the surface slopes and insensitive to the depth of the sample positioning. In this way, the slope calculation is theoretically independent of the sample depth. We call this new deflectometry technique Collimated Phase Measuring Deflectometry (CPMD). With our developed CPMD experimental setup, the measurement is insensitive to the depth of sample positioning, *e.g.*, the measured height dispersion is less than 30 nm RMS within a 10 mm depth range when measuring a 50-mm-diameter spherical mirror with a 200 mm radius of curvature. The merits and limitations of the proposed CPMD technique are discussed, revealing its prospects in practical metrology applications and potential future investigations.

1. Introduction

Freeform optics have gained popularity due to their numerous advantages over traditional optics. One of the benefits of freeform optics is the greater flexibility and control over the shape of optical components to correct various aberrations, leading to improved performance in imaging, illumination, and display applications [1–4]. Freeform optics can also contribute to reducing the size and weight of optical systems, making them more compact and portable. As the field of freeform optics rapidly evolves, we can expect to see more practical applications using freeform optics in various industries, including aerospace, medical imaging, and virtual reality.

To fabricate these freeform optics, it is essential to get accurate in-process metrology feedback for the fabrication process [5,6]. Without such feedback, it is impossible to guide the deterministic fabrication process. This can lead to increasing fabrication time and costs, as well as potential shape errors or defects in the final product. However, it is extremely challenging to accurately measure freeform optics [7]. Classical metrology methods, such as interferometry, may not be well-suited for measuring complex freeform shapes. Specifically, the non-null test condition poses a challenge to classical interferometry which typically uses a transmission flat or a transmission sphere to measure freeform optics. This leads to noticeable measurement errors due to the retrace error, which will reduce the overall measurement accuracy [8].

Currently, two main metrology solutions are used in the interferometry community: Sub-aperture Stitching Interferometry (SSI) [9–11] and Computer-Generated Hologram (CGH) [12–14].

SSI is a technique that enables the flexible extension of the measurement dimension by stitching together sub-aperture measurements with mechanical motions. The retrace error in each sub-aperture is reduced due to the relatively small aperture size, however, as the total number of sub-apertures increases, the stitching error will accumulate leading to a trade-off between the introduced errors in each sub-aperture and the total number of sub-apertures to fully cover the region of interest. Moreover, the mechanical motion error in the transition between sub-apertures must also be considered, as precise control of the mechanical motion is required to minimize this error and ensure accurate reconstruction of the stitched data over the full measurement area.

CGH is a technique used to achieve a null test condition with a proper alignment, where the interference pattern produced by the hologram and the Surface Under Test (SUT) get essentially zero phase difference. This can provide more accurate measurements of the freeform surface. However, one of the major error sources comes from the diffractive wavefront generated from the fabricated CGH. The CGH fabrication

* Corresponding author.
E-mail addresses: huanglei0114@gmail.com, lhuang@bnl.gov (L. Huang).

https://doi.org/10.1016/j.optlaseng.2023.107882
Received 16 August 2023; Received in revised form 24 September 2023; Accepted 3 October 2023
Available online 17 October 2023

error will be directly imprinted onto the surface measurement result. It is also important to note that one CGH plate is typically designed and fabricated specifically to null fringes for one particular surface shape of freeform optics.

In addition to the two metrology techniques mentioned above, Phase Measuring Deflectometry (PMD) is an incoherent, full-field, and slope-based measurement technique that can be used to measure the surface shape of complex freeform optics [15–28]. The PMD technique measures the slopes of the surface at each point using a series of structured patterns illuminated on the surface and observed by a camera. By analyzing the deformation of the captured patterns due to the surface gradients, the surface slopes at each point can be determined. The surface shape can be reconstructed by integrating the measured slopes in two orthogonal directions. The PMD technique has been demonstrated to be effective in measuring specular surfaces [29–32] and transmitted wavefronts [33–36], making it a suitable technique for measuring freeform optics. Some PMD systems use geometric relations to directly calculate the height without slope measurement enabling to measure specular surfaces with discontinuities [37,38]. The system configuration can be flexibly adjusted to meet different measurement dimensions and slope measuring ranges, allowing for customization to meet specific metrology challenges.

However, accurate calibration of a PMD setup is difficult for monoscopic or stereoscopic PMD instruments [39–44]. It is challenging to accurately determine the geometric relations between the screen and the camera(s) in a PMD setup with computer vision methods to guarantee the PMD metrology accuracy to the level that can compete with interferometry.

In addition, the intrinsic height-slope ambiguity in the PMD principle is not fully resolved, although lots of research efforts have been made on this topic [17,20,21,30,32,39,45,46]. This ambiguity arises because the measured slope cannot be uniquely determined when the SUT is placed at different depth positions. As a result, the PMD measurements are sensitive to the depth position of the SUT. To avoid or reduce the error from the height-slope ambiguity, the SUT must be positioned at or close to where the reference mirror was placed during the calibration process. Any deviation from this depth can lead to significant low-frequency errors in the measured surface shape.

The issues in calibration and sample positioning in the PMD technique can limit its ability to accurately measure the low-frequency surface form. As a result, PMD is often used to inspect middle-frequency shape after removing low-order terms [29,36,47,48], to measure relative deformations [49–51], or to detect surface defects [52–54].

In this work, we propose a technique that utilizes the principles of fringe phase measurement and deflectometry to achieve much higher measurement reproducibility. The proposed configuration significantly relaxes the requirement of sample positioning compared to the traditional PMD technique, and it can measure the SUT including the low-frequency form, making it widely applicable for freeform optics measurement. The technique is named Collimated Phase Measuring Deflectometry (CPMD) due to the collimation characteristics of the camera rays, the screen illumination, and the use of the deflectometry principle with fringe phase measurement. The following sections will detail the main idea of the system configuration, measurement method, and experimental verification of this new approach.

2. CPMD principle

In deflectometry, the surface slopes in x- and y-directions, (s_x, s_y), are determined by detecting the deflection of the incident rays on predefined coordinates (x, y). The surface shape distribution z is then reconstructed by integrating the slope values (s_x, s_y) on coordinates (x, y). This process can be expressed as

$$z = \mathrm{intg}(x, y, s_x, s_y), \tag{1}$$

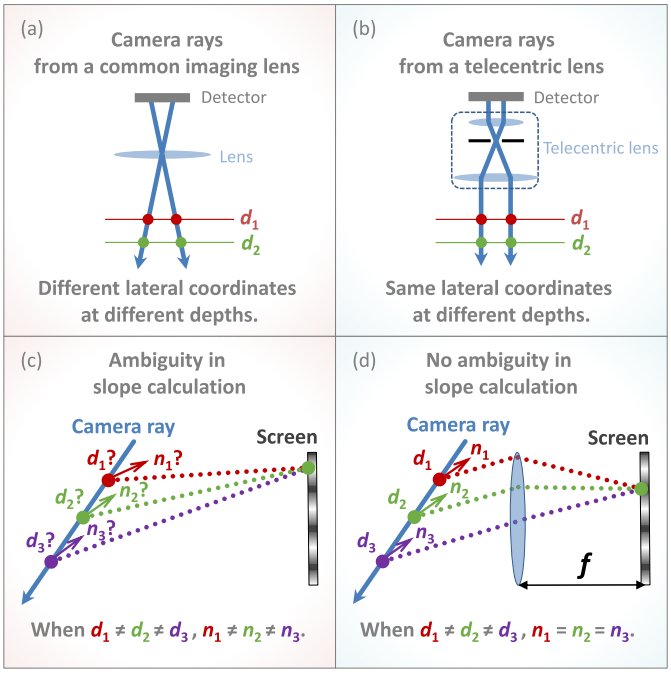

Fig. 1. The two issues in the traditional PMD system and their solutions in CPMD. (a) The lateral coordinates depend on the working distance in the traditional PMD system. (b) Using the telecentric lens, the lateral coordinates are almost independent of the working distance in CPMD. (c) Slope calculation depends on the working distance in the traditional PMD due to the height-slope ambiguity. (d) The slope can be determined almost independently with the working distance.

where intg(·) stands for the integration operation. Many algorithms can perform this numerical integration in Eq. (1) [55–63].

2.1. Consideration of the shape reconstruction dependence on the depth of sample positioning

In the traditional PMD technique, it is challenging to reconstruct the surface shape z with small discrepancies, when the SUT is placed at different depths of sample positioning d. There are two primary reasons.

First, it is because the lateral coordinates (x, y) are dependent on d, expressed as $x(d)$ and $y(d)$. In a monoscopic PMD system using a general imaging lens, the lateral coordinates are calculated from the camera calibration parameters associated with d as illustrated in Fig. 1(a). Since the monoscopic PMD system has no absolute depth detection capability, placing the sample at an unknown depth position different from the reference plane will lead to unspecified errors in x and y. It is one of the reasons that the SUT needs to be placed near the reference plane. In a stereoscopic PMD system, the depth d may have less influence on the determination of x- and y-coordinates (x, y), because depth information can be estimated by minimizing the slope discrepancy between two cameras [15,20,21]. However, the accuracy of d estimation is limited and highly depends on the system calibration, including the geometric calibration and camera calibration. As a result, the error of the lateral coordinates can still vary as a function of d. Once the lateral coordinates (x, y) are functions of d, the shape integration will be influenced by d.

Second, it is because the slopes s_x and s_y are dependent on d, *i.e.*, $s_x(d)$ and $s_y(d)$, due to the height-slope ambiguity as illustrated in Fig. 1(c). Once calculated slopes (s_x, s_y) change with d, the integrated shape z will differ for different d. In a monoscopic PMD system, the retrieved fringe phases (ϕ_x, ϕ_y) will differ when d varies. Therefore, the slopes (s_x, s_y), calculated from fringe phases (ϕ_x, ϕ_y), will be different. In the stereoscopic PMD system, the slopes can be calculated based on

the estimated d. Sometimes this process goes with iterations to best explain the fringe phases retrieved from the captured fringe patterns by the two (or several) cameras. Once again, the consistency of slope measurements at different depths d is highly dependent on the calibration of the system. Although the height-slope ambiguity is partially resolved with the stereoscopic PMD approach, with the computer-vision-based system calibration, it remains challenging to achieve consistent slope results at different d levels. In this sense, surface slopes (s_x, s_y) can still be considered as a function of d.

As a result, the integrated height z becomes dependent on d:

$$z(d) = \mathrm{intg}\Big(x(d), y(d), s_x(d), s_y(d)\Big). \tag{2}$$

This dependence of $z(d)$ in Eq. (2) often results in low-frequency form errors in the final shape reconstruction if the sample is not positioned perfectly at the same depth level where the calibration reference plane was. Due to the introduced low-frequency form errors, the traditional PMD technique is usually used for middle-frequency shape or relative deformation measurement, which strongly limits its wide application.

2.2. CPMD system configuration

With these considerations above, we proposed a new system configuration to tackle these two issues (as shown in Figs. 1(a) and 1(c)) and to calculate lateral coordinates (x, y) and slopes (s_x, s_y) significantly insensitive to d.

To make the lateral coordinates (x, y) independent of d, similar to the Refs. [38,46], an on-axis configuration with a 50/50 beam splitter and a telecentric imaging lens is employed in CPMD. Benefiting from the telecentric lens, the lateral coordinates (x, y) become almost independent of d along the optical axis shown in Fig. 1(b). This can be considered as the "collimation" of the camera rays.

To make the surface slopes (s_x, s_y) independent of d, a Fourier lens is employed in the CPMD system as shown in Fig. 1(d). The screen is placed at the focal plane of the Fourier lens. In this way, similar to the Ref. [64], the Fourier lens can convert the diverging beam from each screen pixel to a parallel wave in a particular direction (also known as a spatial frequency in Fourier optics). This can be considered as the "collimation" of the beam from each screen pixel. These beams in different propagation directions are coded with fringe phases (ϕ_x, ϕ_y). Because the telecentric lens only allows the light parallel to the optical axis to enter the camera, when the beam reflected by the SUT is parallel to the optical axis, it will be exclusively accepted by the telecentric lens. As a result, its intensities are recorded by the camera for phase calculation to decode where the beam comes from on the screen. For a given CPMD system, the fringe phases (ϕ_x, ϕ_y) are majorly sensitive to the local slopes (s_x, s_y) and insensitive to its axial depth d. Therefore, the slope calculation from the fringe phases is theoretically independent of d.

These considerations above are the main ideas in the proposed CPMD technique. The CPMD system configuration is shown in Fig. 2.

In the CPMD configuration, a beam splitter separates the optical paths into the illumination and detection paths. On the illumination path, the screen as a structured-light illumination device is located at the focal plane of the Fourier lens. Together, they provide collimated illumination onto the SUT within a spatial frequency range in the spatial Fourier spectrum. The spatial frequencies of the collimated illumination beam are coded with the fringe phases (ϕ_x, ϕ_y). On the detection path, a camera with a telecentric lens is used to capture the fringe intensities. This on-axis layout can give full play to the advantages of the telecentric lens in that the lateral coordinates are independent of the working distance. In addition, the telecentric lens also acts as a spatial frequency selector. Theoretically, it only allows the beams parallel to the optical axis to enter the camera.

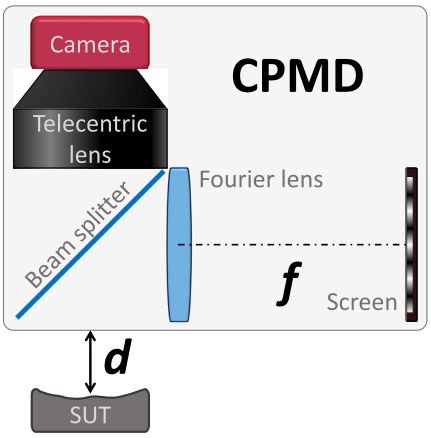

Fig. 2. The CPMD configuration utilizes two key components (a telecentric imaging lens and a Fourier lens) working together to realize the independence between the height reconstruction and the depth of sample positioning in theory.

3. CPMD data processing

After addressing the CPMD configuration, we present the CPMD measurement and data processing procedures. The operation sequence of CPMD is illustrated in Fig. 3.

There are two separate procedures in the CPMD workflow. The first is the camera calibration. Since a telecentric lens is employed in the CPMD configuration, the dedicated calibration method [65,66] determines the parameters of the camera with a telecentric lens. After the camera calibration, the lateral coordinates (x, y) can be determined for each camera pixel (u, v).

The other important procedure is to calculate the local slopes (s_x, s_y) observed by a camera pixel (u, v) at position (x, y) on the SUT. The calculation starts from the fringe patterns captured by the camera. By using the phase shifting method [67] and the multi-frequency phase unwrapping method [68,69], one can retrieve the absolute phase values (ϕ_x, ϕ_y) accurately and robustly. The surface slopes (s_x, s_y) can be calculated by

$$s_x = \frac{p \cdot p_s}{2\pi f}\phi_x, \tag{3}$$

$$s_y = \frac{p \cdot p_s}{2\pi f}\phi_y, \tag{4}$$

where p is the preset fringe period in the unit of screen pixel, p_s is the pixel pitch of the screen monitor, and f is the focal length of the Fourier lens, which is also the distance between the Fourier lens and the screen.

After both the lateral coordinates (x, y) and surface slopes (s_x, s_y) are determined, one can reconstruct the height map z of the SUT with one of the numerical integration methods [55–63]. Once the surface height is reconstructed, it can be used for further data analysis, such as the evaluation of shape errors.

4. Experimental performance evaluation

To verify the proposed CPMD principle, a series of experiments are carried out with our experimental setup. In the sketch shown in Fig. 4(a), the optical path is split into an illumination path and a detection path by a 50/50 beam splitter. As shown in the real setup in Fig. 4(b), fringe patterns in Figs. 4(c) and (d) are displayed on a monitor (HP E24 G4 FHD monitor) to illuminate the specular sample. The Fourier lens is a singlet lens in this experimental setup with a focal length of $f = 500$ mm. A USB3.1 CMOS camera (Allied Vision Alvium 1800 U-811m) attached with a telecentric lens (Edmund Optics®, 0.125X, 2/3″ GoldTL™ Telecentric Lens) is used to capture the fringe patterns reflected by the specular SUT. The field of view is about 60 mm × 60 mm. The camera binning factor is set to be 8×8 in the image acquisition to shorten the exposure time.

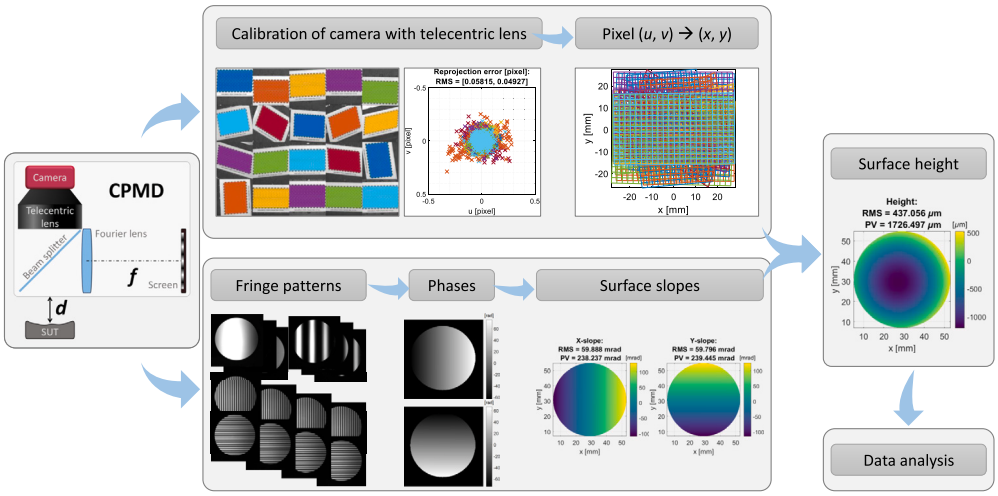

Fig. 3. The CPMD workflow contains two separate threads: the lateral coordinates calculation based on the calibration of the camera with the telecentric lens, and the slope calculation based on the phase measurement from the captured fringe patterns. Eventually, the outputs of these two threads are used for height integration.

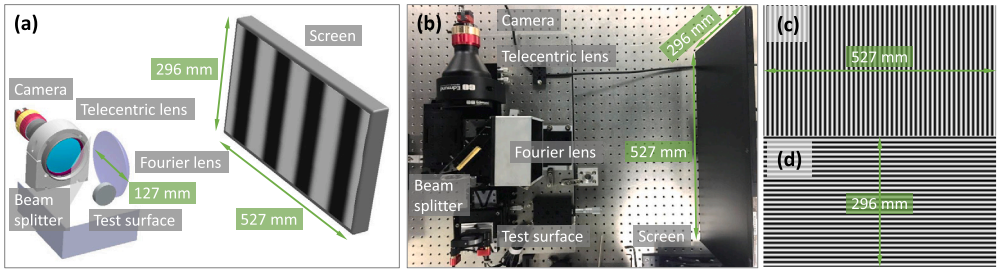

Fig. 4. A sketch (a) and a photo (b) of the CPMD experimental setup, and typical fringe patterns used to display on the screen with (c) x-phase and (d) y-phase.

To apply the multi-frequency phase unwrapping technique, fringe patterns with different frequencies are sequentially displayed on the screen. In our experiment, the fringe frequency ratio is typically set as 7, yielding patterns with 1, 7, or 49 fringes in the longest dimension. The fringe periods in x and y-directions are identical. These fringe patterns are 4-, 4-, or 16-step phase shifted, respectively, and the captured images are used to calculate the x- or y-phases of the fringes.

4.1. Repeatability test

The repeatability of the CPMD measurement is first studied by continuously measuring a flat mirror. The measurement is repeated 30 times. Taking the average of these measurements as the baseline, one can calculate the dispersion of each measurement in slope or height. From the repeatability test results in Fig. 5, we can see the slopes and height measurements are very repeatable. The Root Mean Square (RMS) values of the slope dispersion are about 6 μrad for both x- and y-slopes as shown in Figs. 5(a) and 5(b).

From the height repeatability result in Fig. 5(c), although a small drift in curvature is observed, the RMS values of the de-tilted height dispersion are less than 6 nm. The dispersion distribution of the x-slope, the y-slope, and the de-tilted height of measurements #5, #15, and #25 are shown in Figs. 5(d), 5(e), and 5(f). This provides a baseline for other performance evaluations.

4.2. Verification of the insensitivity to the sample axial position

The primary objective of our experiment is to verify whether the slope calculations in the proposed CPMD exhibit reduced sensitivity towards variations in the sample position.

To avoid potential biases from one-sided cognitive perspectives, the sensitivity to the sample distance is studied by measuring three different types of test mirrors (a flat mirror, a spherical mirror, and a freeform mirror). For each case, we shift the test mirror in the axial direction with a 1 mm step size within ±5 mm from the nominal plane of the best focus. The height reconstruction results are compared with that measured at the nominal plane. A linear piezo stage (PI LPS-65) is aligned to the optical axis of the camera. It carries the test sample for this 10 mm axial translation precisely.

Considering the control of this error contribution to the overall reconstruction error, we set the error due to the depth variation as 30 nm RMS as an error budget threshold to evaluate the CPMD measurement results for different sample positions.

4.2.1. Case 1: evaluation with a flat mirror

A 50-mm-diameter flat mirror is measured when $\Delta d = \pm 5$ mm with a 1 mm step size to demonstrate the slope calculation is insensitive to the distance change. X-slope profiles of the center line in the horizontal direction at different depths are shown in Fig. 6(a). The differences of the x-slope profiles from the results at the nominal position $\Delta d =$ 0 mm are small and almost at the noise level as shown in Fig. 6(b). Fig. 6(c) shows y-slope profiles of the center line in the vertical direction at different depths, and their small differences from the y-slope profile at the nominal depth are shown in Fig. 6(d).

As demonstrated in Fig. 7, if the height map of the flat mirror at the nominal position is used as the benchmark, the measured height differences (with the piston, tip, and tilt removed only) at different depth locations are below 10 nm RMS in this 10 mm depth range. Compared with the traditional PMD (almost 4000 nm RMS height error in 3 mm depth difference) or even PMD using a telecentric lens [46] (>20 nm RMS height error in 3 mm depth difference), the proposed CPMD measurement of a flat mirror is remarkably insensitive to the sample position.

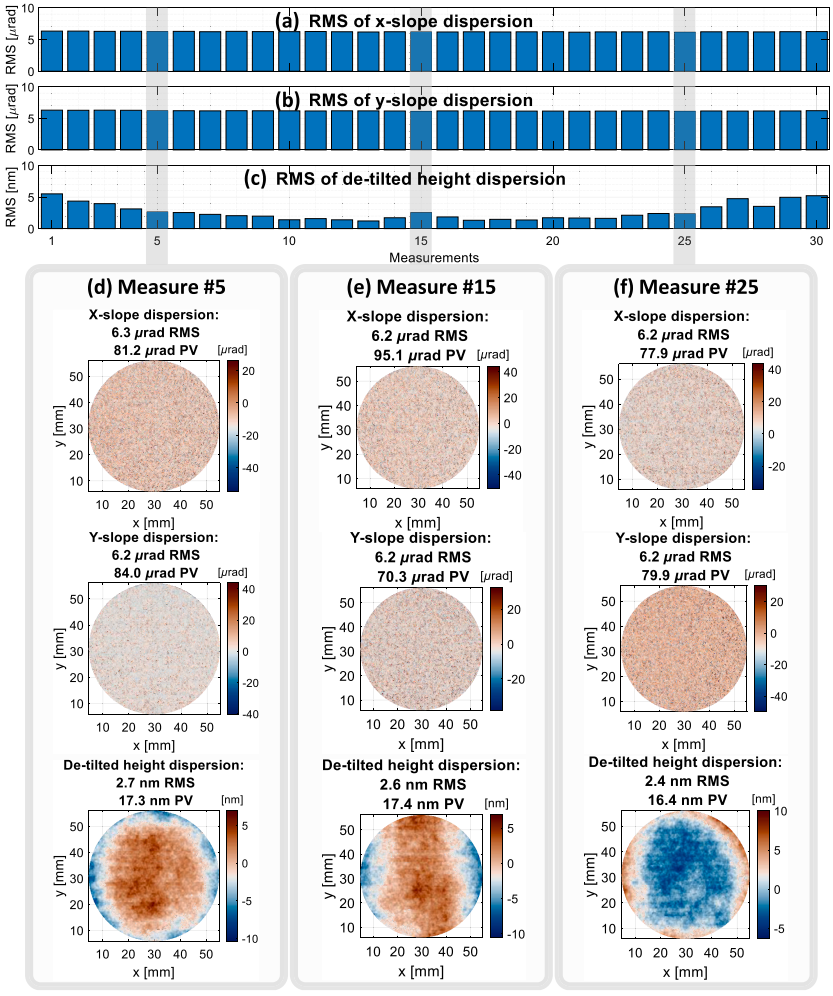

Fig. 5. The CPMD measurement is repeatable. With our experiment condition and the parameter settings, the measurement repeatability is around 6 μrad RMS for both *x*-slope (a) and *y*-slope (b) and below 6 nm RMS for de-tilted height (c). The maps of the dispersion in measurements #5 (d), #15 (e), and #25 (f) are given to show the distribution of the dispersion.

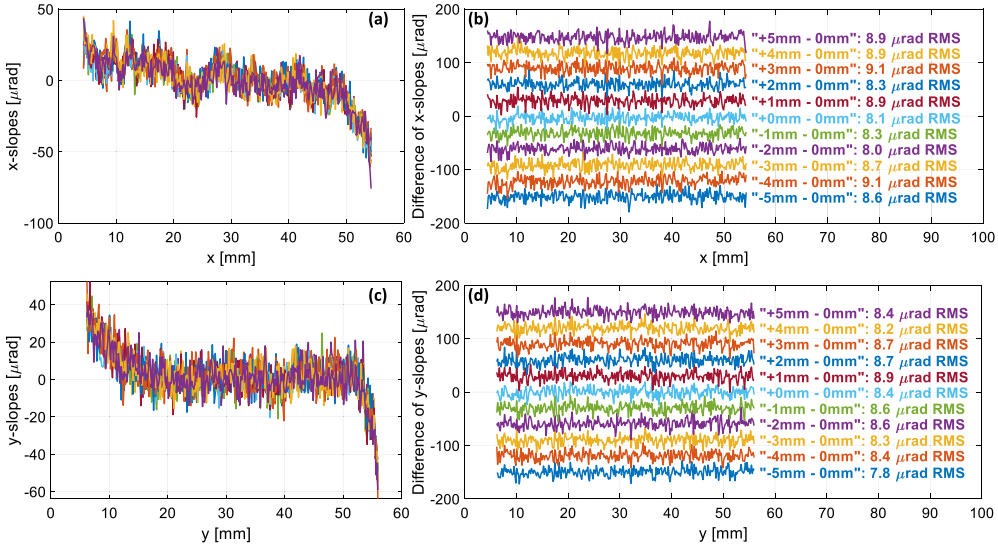

Fig. 6. Slope measurement results of a flat mirror are insensitive to the depth of sample positioning within a 10 mm range. (a) X-slope profiles at different depths, (b) difference of x-slopes compared to the slope profile measured at the nominal depth position (vertically shifted for clearer data comparison), (c) y-slope profiles at different depths, and (d) difference of y-slopes compared to the slope profile measured at the nominal depth position (vertically shifted for clearer data comparison).

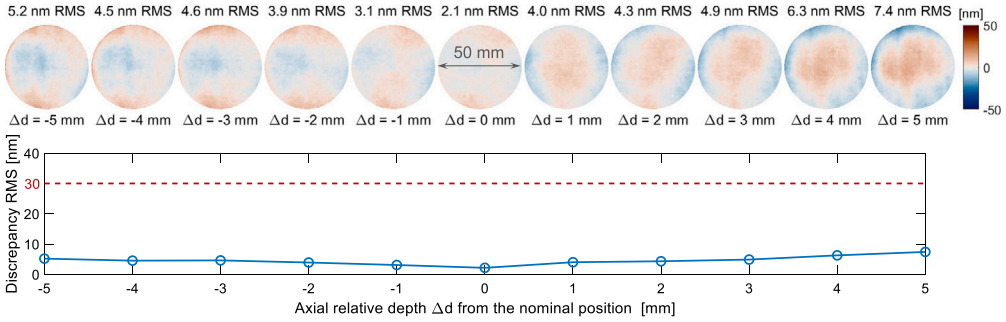

Fig. 7. The reconstruction of a flat mirror is insensitive to the depth change within a 10 mm range using the CPMD technique. The top panel displays the discrepancy maps of the measurements at different depths, and the bottom plot shows the RMS values of the discrepancies *v.s.* the axial relative depth from the nominal position.

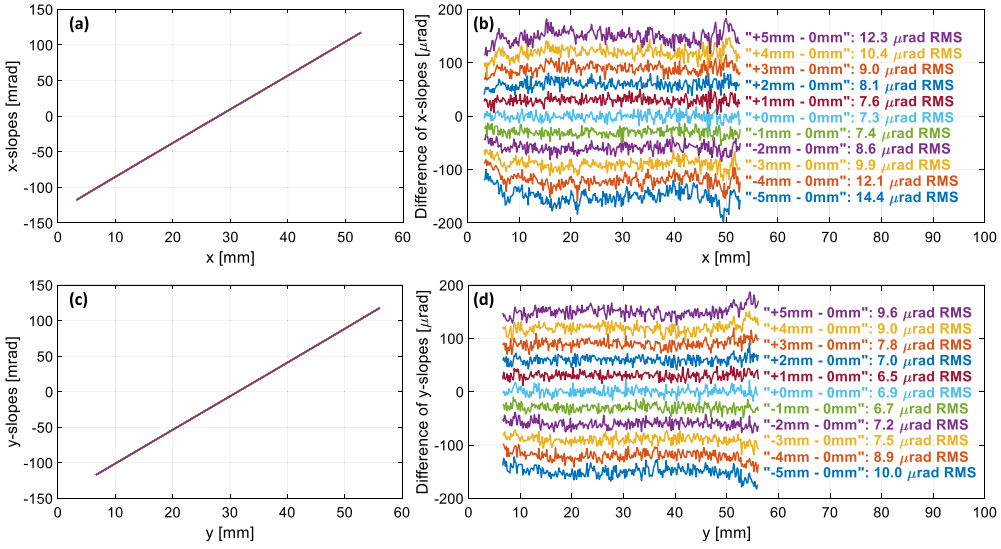

Fig. 8. Slope measurement results of a spherical mirror (RoC≈ 200 mm) are insensitive to the depth of sample positioning within a 10 mm range. (a) X-slope profiles, (b) the differences of measured x-slopes at the nominal depth position (vertically shifted for clearer data comparison), (c) y-slope profiles, and (d) the differences of measured y-slopes at the nominal depth position (vertically shifted for clearer data comparison).

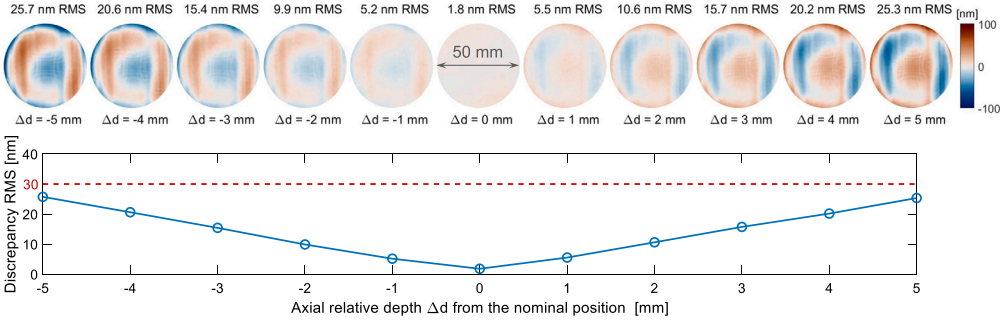

Fig. 9. The reconstruction of a spherical mirror (RoC ≈ 200 mm) is insensitive to the depth change within a 10 mm range using the CPMD technique. The top panel displays the discrepancy maps of the measurements at different depths, and the bottom plot shows the RMS values of discrepancies *v.s.* the axial depth from the nominal position.

4.2.2. Case 2: evaluation with a spherical mirror

Similarly, a 50-mm-diameter spherical mirror with a Radius of Curvature (RoC) of about 200 mm is tested when moved at different axial positions with Δd in a range of 10 mm. The slope profiles and their relative differences are shown in Fig. 8.

From the slope profile in Figs. 8(a) and (c), we can see that although the total slope ranges are more than 200 mrad in both x- and y-directions, the slope differences between measures at different axial depth location are still small ($<$ 15 μrad RMS) as shown in Figs. 8(b) and (d).

Fig. 9 shows a spherical aberration varying along the axial direction. It is primarily due to the spherical aberration of the Fourier lens used in the system. It can be improved by replacing it with a better aspherical lens. Nevertheless, the introduced shape change (with the piston, tip, and tilt removed only) due to the 10 mm distance change is still below the 30 nm RMS error budget.

4.2.3. Case 3: evaluation with a freeform mirror

An elliptical cylindrical mirror with a surface size of 45 mm × 30 mm and its local RoC varying from 43.2 m to 10.2 m is tested as an

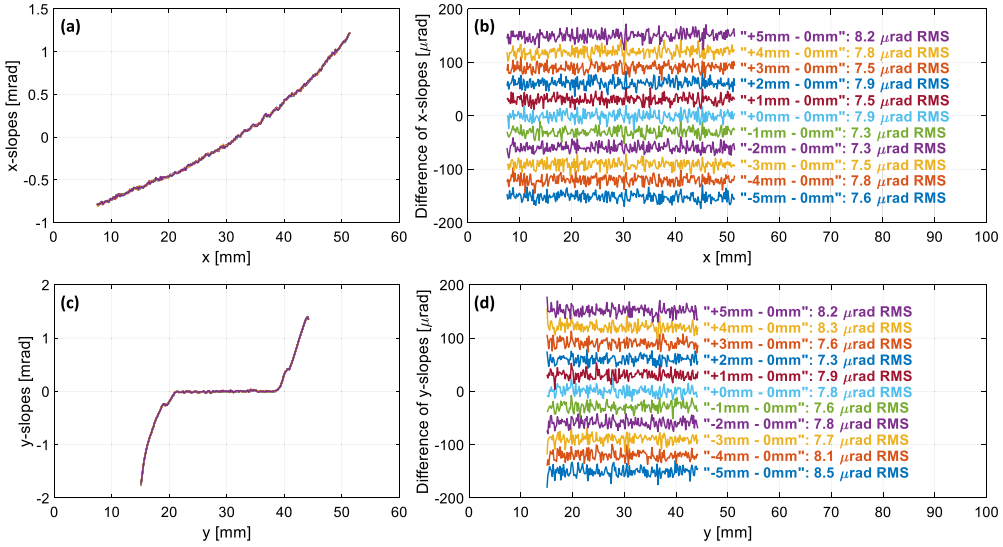

Fig. 10. Slope measurement results of a 45 mm × 30 mm elliptical cylindrical mirror are insensitive to the depth of sample positioning within a 10 mm range. (a) X-slope profiles, (b) the differences of x-slopes compared to the slope profile measured at the nominal depth position (vertically shifted for clearer data comparison), (c) y-slope profiles, and (d) the difference of y-slopes compared to the slope profile measured at the nominal depth position (vertically shifted for clearer data comparison).

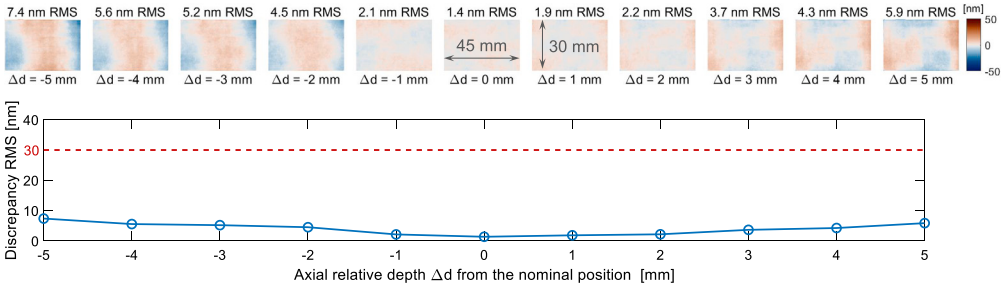

Fig. 11. The CPMD measurement of a 45 mm × 30 mm elliptical cylindrical mirror is insensitive to the 10 mm depth change. The top panel displays the discrepancy maps of measurements at different depths, and the bottom plot shows the RMS values of the discrepancies *v.s.* the axial relative depth from the nominal position.

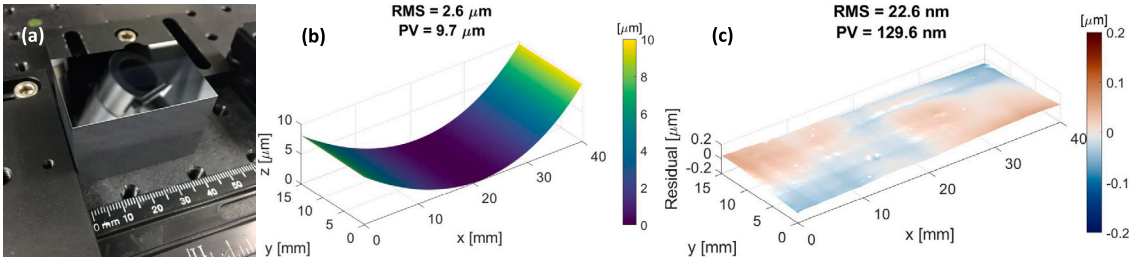

Fig. 12. An elliptical cylindrical mirror is measured with the CPMD technique. (a) Photo of the elliptical cylindrical mirror, (b) the height map of the optical area measured by the CPMD technique, and (c) the residual height after the best fitting of the target elliptical cylinder.

example of freeform optics. This freeform mirror is measured at every 1 mm within a 10 mm axial depth range. The slope profiles and the relative differences are shown in Fig. 10. The x- or y-slope differences are less than 10 μrad RMS when measuring the around 2 mrad slope range freeform mirror at different depth locations.

The measured shape variation (with the piston, tip, and tilt removed only) as shown in Fig. 11 is below 10 nm RMS in this 10 mm axial position change. This is an excellent result which demonstrates that the CPMD technique mitigates the influence from the axial sample positions.

These three examples demonstrate that our CPMD experimental setup is insensitive to the 10 mm axial sample position variation (shape discrepancy less than 30 nm RMS in a 60 mm × 60 mm field of view). In practical measurements, a depth tolerance of 10 mm is a reasonable and decent range to place the test surface. This is the main advantage of using the CPMD technique compared to the traditional PMD technique.

4.3. Measurements examples with the CPMD technique

In this section, we demonstrate some CPMD measurement examples to demonstrate the feasibility of the proposed CPMD technique in practical measurement. In these demonstrations, the samples are placed without precise depth adjustment. A flat mirror is used as a reference measurement to remove systematic errors.

The first test mirror is a high-precision synchrotron mirror with a 40 mm × 15 mm optical area shown in Fig. 12(a). This mirror was

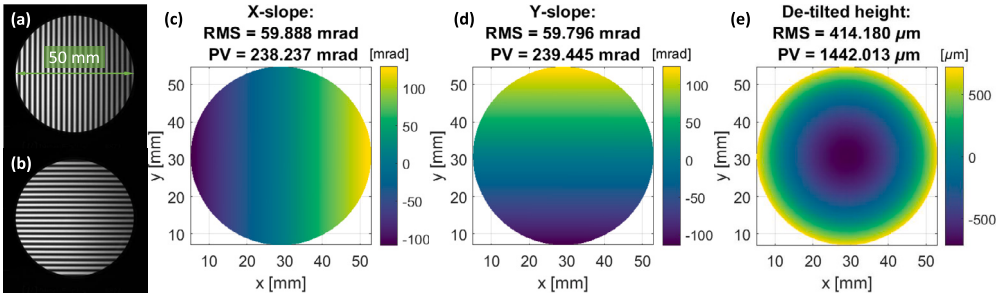

Fig. 13. A 50-mm-diameter 100-mm-EFL spherical mirror is measured with the CPMD technique. (a) An x-fringe pattern and (b) a y-fringe pattern captured by the camera, (c) the measured x-slope and (d) the y-slope, and (d) the measured de-tilted height result.

fabricated using the NSLS-II Ion Beam Figuring (IBF) instrument [70]. In its optical area, the mirror surface is in an elliptical cylindrical shape with an object distance of 8.555 m, an image distance of 0.05 m, and a grazing angle of 4 mrad. Its tangential RoC changes from 41.0 m to 11.6 m. This mirror is inspected by using the NSLS-II stitching interferometer [71]. It has been confirmed that the residual height from the target elliptical cylindrical shape is about 1 nm RMS. This is hence an excellent freeform sample to check the accuracy of our CPMD experimental setup.

From the measurement results shown in Fig. 12 (b), we see that CPMD can successfully measure the mirror surface shape. The optical area is cropped out and fitted with the target ellipse. After the best fitting with the target elliptical cylinder, the residual height in Fig. 12(c) is 22.6 nm RMS and 129.6 nm PV, which shows the measurement accuracy of the developed CPMD experimental setup when measuring such freeform optics without any dedicated sample position adjustment.

The second test sample is a 50-mm-diameter spherical mirror with a 100 mm Effective Focal Length (EFL) produced by Edmund Optics. Figs. 13(a) and 13(b) show two typical fringe patterns captured by the camera. The x- and y-slope measurement results are presented in Figs. 13(c) and 13(d). The RoC is calculated as 200.378 mm from the height measurement data shown in Fig. 13(e).

The third example is a "magic mirror" fabricated by etching a flat mirror surface with a designed pattern using the NSLS-II IBF instrument [70]. Figs. 14(a) and 14(b) show the interferograms before and after the IBF process. Due to the local curvature variation on the etched surface, the designed pattern can show up via reflection of the illumination (*e.g.*, under the sunshine) as demonstrated in Fig. 14(c). This mirror is measured by both a Fizeau interferometer and our CPMD experimental setup. In this way, we can compare these two measurement results. Two typical x- and y-fringe patterns captured in the CPMD measurement are displayed in Figs. 14(d) and 14(e). The x- and y-slope measurement results of the IBF-processed central area are shown in Figs. 14(f) and 14(g). After the point cloud registration, the height results of the CPMD and the Fizeau interferometer are displayed in Fig. 14(h) by shifting the Fizeau results in the x-axis for better comparison. The height difference between these two measurements is 15.1 nm RMS and 120.0 nm PV, as shown in Fig. 14(h).

These three metrology examples (see the supplementary material **Visualization 1** for the captured fringe patterns) demonstrate the feasibility of the CPMD technique in measuring specular surfaces. One thing to be highlighted is that there was no careful adjustment of the sample position before these measurements.

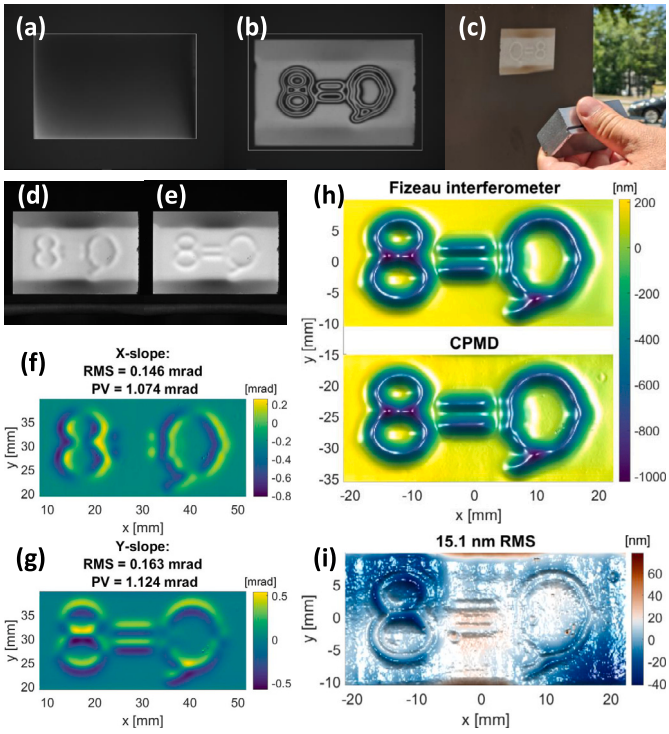

Fig. 14. A "magic mirror" is measured with the CPMD technique and compared with the height result measured using a Fizeau interferometer. The Fizeau interferograms of the mirror before (a) and after (b) the IBF process. (c) The "magic mirror" reflects the etched pattern under the sunshine. Fringe patterns in x- (d) and y-directions (e) are captured when this mirror is measured by using the CPMD technique to calculate the x- (f) and y-slopes (g). The height maps measured with the CPMD technique and the Fizeau interferometer (h) are compared by showing their difference (i).

5. Discussion

The proposed CPMD method eliminates the height-slope ambiguity in theory. The experiment results show that slope measurement is almost insensitive to the sample axial position. Several experiments with different sample shapes demonstrate that the reconstruction difference is below 30 nm RMS in a ±5 mm depth range. This advantage of measurement self-consistency is important for many metrology applications. More significantly, it is critical for applications that require low-frequency form information. The field of view in our experimental setup is currently about 60 mm × 60 mm. To enlarge the field of view, larger optical elements, including the telecentric lens, the beam splitter, and the Fourier lens, are required, which may increase the cost of the measurement system. Therefore, data stitching could be a good option to measure a sample larger than the field of view.

The experiment results indicate that, compared to the Fizeau interferometer with a transmission flat, the proposed CPMD can measure a much more extensive slope-measuring range. Compared to the Fizeau with a transmission sphere, the CPMD technique has flexible slope measuring capability in the two orthogonal directions, which is convenient for freeform optics metrology. Therefore, it has the potential to tackle the challenges of measuring freeform optics. There is a side effect of using a Fourier lens to solve the height-slope ambiguity. Similarly to the interferometer, the retrace error is introduced into the measurement result. To further improve the measurement accuracy, a better lens with

less aberration is preferred and the calibration of the retrace error is mandatory to correct this systematic error. Our possible future work will focus on lens optimization and the retrace error calibration for the CPMD technique.

Although we demonstrate mirror measurements by using the CPMD technique with a reflection setup, the idea of using the "collimated" camera rays and the "collimated" structured-light illumination in the proposed CPMD technique can be easily applied in measuring the transmitted wavefront through the optical lenses under test.

6. Conclusion

We have presented the CPMD (Collimated Phase Measuring Deflectometry) technique as a novel solution to address the height-slope ambiguity issue present in the traditional PMD method. By using a telecentric imaging lens and a Fourier lens in an on-axis optical layout, the proposed CPMD technique makes the fringe phase values sensitive only to the surface normal and not affected by the sample axial position in theory. Therefore, the slope calculation becomes theoretically independent of the sample axial position reducing the requirement for a precise sample position adjustment. Our experimental results validate that the CPMD technique mitigates the influence of the sample axial position. The measurement results become almost insensitive to the sample axial position with less than 30 nm RMS height differences within a ±5 mm axial displacement.

This advantage of the CPMD method makes it suitable for measuring freeform optics. Measurement examples demonstrate that the CPMD technique is a convenient metrology solution for freeform specular surfaces, including the low-frequency form. The CPMD technique provides a promising solution for the height-slope ambiguity issue in deflectometry, and it is applicable to measure freeform optics in many applications.

To improve the measurement accuracy, future work will focus on the optics design and fabrication, and developing a retrace error calibration approach for the CPMD technique.

CRediT authorship contribution statement

Lei Huang: Conceptualization, Methodology, Software, Writing - Original draft preparation. **Tianyi Wang:** Software, Investigation, Writing - Reviewing and Editing. **Corey Austin:** Data curation, Investigation, Writing - Reviewing and Editing. **Lukas Lienhard:** Mechanical design. **Yan Hu:** Methodology, Writing - Reviewing and Editing. **Chao Zuo:** Supervision, Writing - Reviewing and Editing. **Daewook Kim:** Writing - Reviewing and Editing. **Mourad Idir:** Supervision, Writing - Reviewing and Editing.

Funding

This work was supported by the NSLS-II Facility Improvement Project (21153), DOE Office of Science (DE-SC0012704), and the Accelerator and Detector Research Program, part of the Scientific User Facility Division of the Basic Energy Science Office of the U.S. Department of Energy (DOE), under the Field Work Proposal No. FWP-PS032.

Declaration of competing interest

The authors declare the following financial interests/personal relationships which may be considered as potential competing interests: Lei Huang, Tianyi Wang, and Mourad Idir have patent pending to declare a patent application to be filed by Brookhaven Science Associates, LLC under a prime contract with the U.S. Department of Energy DE-SC0012704.

Data availability

Data underlying the results presented in this paper are not publicly available at this time but may be obtained from the authors upon reasonable request.

Acknowledgement

The authors want to thank Daodang Wang in the Wyant College of Optical Sciences at the University of Arizona for helpful discussions and Philip Boccabella in the Research & Development Group of NSLS-II for the mechanical machining.

This research used resources of the National Synchrotron Light Source II, a U.S. Department of Energy (DOE) Office of Science User Facility, operated for the DOE Office of Science by Brookhaven National Laboratory under Contract No. DE-SC0012704.

Appendix A. Supplementary material

Supplementary material related to this article can be found online at https://doi.org/10.1016/j.optlaseng.2023.107882.

References

[1] Rolland JP, Davies MA, Suleski TJ, Evans C, Bauer A, Lambropoulos JC, et al. Freeform optics for imaging. Optica 2021;8:161–76.
[2] Tang Z, Gross H. Extended aberration analysis in symmetry-free optical systems - part I: method of calculation. Opt Express 2021;29:39967–82.
[3] Tang Z, Gross H. Extended aberration analysis in symmetry-free optical systems - part II: evaluation and application. Opt Express 2021;29:42020–36.
[4] Falaggis K, Rolland J, Duerr F, Sohn A. Freeform optics: introduction. Opt Express 2022;30:6450–5.
[5] Blalock T, Medicus K, Nelson JD. Fabrication of freeform optics. In: Fähnle OW, Williamson R, Kim DW, editors. Optical manufacturing and testing XI. Optical manufacturing and testing, vol. 9575. International Society for Optics and Photonics (SPIE); 2015. p. 95750H.
[6] Shimizu Y, Chen L-C, Kim DW, Chen X, Li X, Matsukuma H. An insight into optical metrology in manufacturing. Meas Sci Technol 2021;32:042003.
[7] Chen S, Xue S, Zhai D, Tie G. Measurement of freeform optical surfaces: trade-off between accuracy and dynamic range. Laser Photonics Rev 2020;14:1900365.
[8] Shahinian H, Hovis CD, Evans CJ. Effect of retrace error on stitching coherent scanning interferometry measurements of freeform optics. Opt Express 2021;29:28562–73.
[9] Supranowitz C, Lormeau J-P, Maloney C, Murphy P, Dumas P. Freeform metrology using subaperture stitching interferometry. In: Kovacicinova J, editor. Optics and measurement international conference 2016, vol. 10151. International Society for Optics and Photonics (SPIE); 2016. p. 101510D.
[10] Piché F, Maloney C, VanKerkhove S, Supranowicz C, Dumas P, Donohue K. New high-precision deep concave optical surface manufacturing capability. In: Bentley JL, Stoebenau S, editors. Optifab 2017, vol. 10448. SPIE; 2017. p. 104480H.
[11] Felkel EM. Zygo corporation: measure small aspheres & freeforms with ZYGO's 3D, non-contact COMPASS. In: Chair C, editor. SPIE exhibition product demonstrations, vol. 11716. International Society for Optics and Photonics (SPIE); 2021. p. 117162J.
[12] Su P, Kang G, Tan Q, Jin G. Estimation and optimization of computer-generated hologram in null test of freeform surface. Chin Opt Lett 2009;7:1097–100.
[13] Scheiding S, Beier M, Zeitner U-D, Risse S, Gebhardt A. Freeform mirror fabrication and metrology using a high performance test CGH and advanced alignment features. In: von Freymann G, Schoenfeld WV, Rumpf RC, editors. Advanced fabrication technologies for micro/nano optics and photonics VI, vol. 8613. International Society for Optics and Photonics (SPIE); 2013. p. 86130J.
[14] Zhao C. Computer-generated hologram for optical testing: a review. In: Mahajan VN, Kim D, editors. Tribute to James C. Wyant: the extraordinaire in optical metrology and optics education, vol. 11813. International Society for Optics and Photonics (SPIE); 2021. p. 118130K.
[15] Knauer MC, Kaminski J, Hausler G. Phase measuring deflectometry: a new approach to measure specular free-form surfaces. In: Osten W, Takeda M, editors. Optical metrology in production engineering, vol. 5457. International Society for Optics and Photonics (SPIE); 2004. p. 366–76.
[16] Bothe T, Li W, von Kopylow C, Juptner WPO. High-resolution 3D shape measurement on specular surfaces by fringe reflection. In: Osten W, Takeda M, editors. Optical metrology in production engineering, vol. 5457. International Society for Optics and Photonics (SPIE); 2004. p. 411–22.
[17] Petz M, Tutsch R. Reflection grating photogrammetry: a technique for absolute shape measurement of specular free-form surfaces. In: Stahl HP, editor. Optical manufacturing and testing VI, vol. 5869. International Society for Optics and Photonics (SPIE); 2005. p. 58691D.

[18] Tang Y, Su X, Liu Y, Jing H. 3d shape measurement of the aspheric mirror by advanced phase measuring deflectometry. Opt Express 2008;16:15090–6.
[19] Zhao W, Su X, Liu Y, Zhang Q. Testing an aspheric mirror based on phase measuring deflectometry. Opt Eng 2009;48:103603.
[20] Werling S, Mai M, Heizmann M, Beyerer J. Inspection of specular and partially specular surfaces. Metrol. Meas. Syst. 2009;16:415–31.
[21] Balzer J, Werling S. Principles of shape from specular reflection. Measurement 2010;43:1305–17.
[22] Huang L, Ng CS, Asundi AK. Dynamic three-dimensional sensing for specular surface with monoscopic fringe reflectometry. Opt Express 2011;19:12809–14.
[23] Zhang Z, Wang Y, Huang S, Liu Y, Chang C, Gao F, et al. Three-dimensional shape measurements of specular objects using phase-measuring deflectometry. Sensors 2017;17.
[24] Huang L, Idir M, Zuo C, Asundi A. Review of phase measuring deflectometry. Opt Lasers Eng 2018;107:247–57.
[25] Xu Y, Gao F, Jiang X. A brief review of the technological advancements of phase measuring deflectometry. PhotoniX 2020;1:1–10.
[26] Burke Jan, Pak Alexey, Höfer Sebastian, Ziebarth Mathias, Roschani Masoud, Beyerer Jürgen. Deflectometry for specular surfaces: an overview. Adv. Opt. Technol. 2023;12. https://doi.org/10.3389/aot.2023.1237687. https://www.frontiersin.org/articles/10.3389/aot.2023.1237687.
[27] Nguyen MT, Ghim Y-S, Rhee H-G. DYnet++: A deep learning based single-shot phase-measuring deflectometry for the 3D measurement of complex free-form surfaces. IEEE Trans Ind Electron 2023:1–10.
[28] Wu Z, Wang J, Jiang X, Fan L, Wei C, Yue H, et al. High-precision dynamic three-dimensional shape measurement of specular surfaces based on deep learning. Opt Express 2023;31:17437–49.
[29] Su P, Parks RE, Wang L, Angel RP, Burge JH. Software configurable optical test system: a computerized reverse Hartmann test. Appl Opt 2010;49:4404–12.
[30] Häusler G, Faber C, Olesch E, Ettl S. Deflectometry vs. interferometry. In: Lehmann PH, Osten W, Albertazzi A, editors. Optical measurement systems for industrial inspection VIII, vol. 8788. International Society for Optics and Photonics (SPIE); 2013. p. 87881C.
[31] Burke J, Li W, Heimsath A, von Kopylow C, Bergmann R. Qualifying parabolic mirrors with deflectometry. J Eur Opt Soc, Rapid Publ 2013;8.
[32] Huang L, Xue J, Gao B, McPherson C, Beverage J, Idir M. Modal phase measuring deflectometry. Opt Express 2016;24:24649–64.
[33] Wang D, Xu P, Gong Z, Xie Z, Liang R, Xu X, et al. Transmitted wavefront testing with large dynamic range based on computer-aided deflectometry. J Opt 2018;20:065705.
[34] Wang D, Xu P, Wu Z, Fu X, Wu R, Kong M, et al. Simultaneous multisurface measurement of freeform refractive optics based on computer-aided deflectometry. Optica 2020;7:1056–64.
[35] Wang C, Chen N, Heidrich W. Towards self-calibrated lens metrology by differentiable refractive deflectometry. Opt Express 2021;29:30284–95.
[36] Chen Z, Zhao W, Zhang Q, Peng J, Hou J. Wavefront measurement of a multilens optical system based on phase measuring deflectometry. Chin Opt Lett 2023;21:041201.
[37] Liu Y, Huang S, Zhang Z, Gao N, Gao F, Jiang X. Full-field 3d shape measurement of discontinuous specular objects by direct phase measuring deflectometry. Sci Rep 2017;7:10293.
[38] Niu Z, Gao N, Zhang Z, Gao F, Jiang X. 3D shape measurement of discontinuous specular objects based on advanced PMD with bi-telecentric lens. Opt Express 2018;26:1615–32.
[39] Olesch E, Faber C, Häusler G. Deflectometric self-calibration for arbitrary specular surfaces. In: Proc. DGao; 2011.
[40] Xiao Y-L, Su X, Chen W. Flexible geometrical calibration for fringe-reflection 3d measurement. Opt Lett 2012;37:620–2.
[41] Han H, Wu S, Song Z. An accurate calibration means for the phase measuring deflectometry system. Sensors 2019;19.
[42] Xu X, Zhang X, Niu Z, Wang W, Zhu Y, Xu M. Self-calibration of in situ monoscopic deflectometric measurement in precision optical manufacturing. Opt Express 2019;27:7523–36.
[43] Allgeier S, Gengenbach U, Köhler B, Reichert K-M, Hagenmeyer V. Reproducibility of two calibration procedures for phase-measuring deflectometry. In: Morris MBN, Creath K, Porras-Aguilar R, editors. Interferometry XX, vol. 11490. International Society for Optics and Photonics (SPIE); 2020. p. 114900G.
[44] Wang R, Li D, Zhang X. Systematic error control for deflectometry with iterative reconstruction. Measurement 2021;168:108393.
[45] Graves LR, Choi H, Zhao W, Oh CJ, Su P, Su T, et al. Model-free deflectometry for freeform optics measurement using an iterative reconstruction technique. Opt Lett 2018;43:2110–3.
[46] Yue H-M, Wu Y-X, Song Y-P, Liu Y. Solution to the slope-height ambiguity problem in phase measuring deflectometry based on a co-axial telecentric optical path. Meas Sci Technol 2020;31:045007.
[47] Huang L, Wong JX, Asundi A. Specular 3D shape measurement with a compact fringe reflection system. In: Quan C, Qian K, Asundi A, editors. International conference on optics in precision engineering and nanotechnology (icOPEN2013), vol. 8769. International Society for Optics and Photonics (SPIE); 2013. p. 87691K.
[48] Blalock T, Cox B, Myer B. Measurement of mid-spatial frequency errors on freeform optics using deflectometry. In: Lehmann P, Osten W, Jr. AAG, editors. Optical measurement systems for industrial inspection XI, vol. 11056. International Society for Optics and Photonics, SPIE; 2019. p. 110561H.
[49] Huang L, Seng Ng C, Krishna Asundi A. Fast full-field out-of-plane deformation measurement using fringe reflectometry. Opt Lasers Eng 2012;50:529–33.
[50] Li W, Huke P, Burke J, von Kopylow C, Bergmann RB. Measuring deformations with deflectometry. In: Creath K, Burke J, Schmit J, editors. Interferometry XVII: techniques and analysis, vol. 9203. International Society for Optics and Photonics (SPIE); 2014. p. 92030F.
[51] O'donoughue P, Gautier F, Meteyer E, Durand-Texte T, Secail-Geraud M, Foucart F, et al. Comparison of three full-field optical measurement techniques applied to vibration analysis. Sci Rep 2023;13:3261.
[52] Guan J, Li J, Yang X, Chen X, Xi J. Defect detection method for specular surfaces based on deflectometry and deep learning. Opt Eng 2022;61:061407.
[53] Zhou Q, Chen R, Huang B, Xu W, Yu J. Deepinspection: deep learning based hierarchical network for specular surface inspection. Measurement 2020;160:107834.
[54] Fan L, Wu Z, Wang J, Wei C, Yue H, Liu Y. Deep learning-based phase measuring deflectometry for single-shot 3d shape measurement and defect detection of specular objects. Opt Express 2022;30:26504–18.
[55] Southwell W. Wave-front estimation from wave-front slope measurements. J Opt Soc Am 1980;70:998–1006.
[56] Ettl S, Kaminski J, Knauer MC, Häusler G. Shape reconstruction from gradient data. Appl Opt 2008;47:2091–7.
[57] Bon P, Monneret S, Wattellier B. Noniterative boundary-artifact-free wavefront reconstruction from its derivatives. Appl Opt 2012;51:5698–704.
[58] Li G, Li Y, Liu K, Ma X, Wang H. Improving wavefront reconstruction accuracy by using integration equations with higher-order truncation errors in the Southwell geometry. J Opt Soc Am A 2013;30:1448–59.
[59] Huang L, Idir M, Zuo C, Kaznatcheev K, Zhou L, Asundi A. Comparison of two-dimensional integration methods for shape reconstruction from gradient data. Opt Lasers Eng 2015;64:1–11.
[60] Huang L, Xue J, Gao B, Zuo C, Idir M. Spline based least squares integration for two-dimensional shape or wavefront reconstruction. Opt Lasers Eng 2017;91:221–6.
[61] Huang L, Xue J, Gao B, Zuo C, Idir M. Zonal wavefront reconstruction in quadrilateral geometry for phase measuring deflectometry. Appl Opt 2017;56:5139–44.
[62] Swanson R, Lamb M, Correia C, Sivanandam S, Kutulakos K. Wavefront reconstruction and prediction with convolutional neural networks. In: Close LM, Schreiber L, Schmidt D, editors. Adaptive optics systems VI, vol. 10703. International Society for Optics and Photonics (SPIE); 2018. p. 107031F.
[63] Gong X, Sun Z, Lv Y, Jiang Z, Xu X. Improved difference model applied in the Fourier-transform-based integration method based on Taylor theory. Appl Opt 2020;59:6476–83.
[64] Seßner R. Richtungscodierte Deflektometrie durch Telezentrie. Ph.D. thesis. Friedrich-Alexander-Universität Erlangen-Nürnberg (FAU); 2009.
[65] Chen Z, Liao H, Zhang X. Telecentric stereo micro-vision system: calibration method and experiments. Opt Lasers Eng 2014;57:82–92.
[66] Hu Y, Chen Q, Feng S, Tao T, Asundi A, Zuo C. A new microscopic telecentric stereo vision system - calibration, rectification, and three-dimensional reconstruction. Opt Lasers Eng 2019;113:14–22.
[67] Zuo C, Feng S, Huang L, Tao T, Yin W, Chen Q. Phase shifting algorithms for fringe projection profilometry: a review. Opt Lasers Eng 2018;109:23–59.
[68] Zhao H, Chen W, Tan Y. Phase-unwrapping algorithm for the measurement of three-dimensional object shapes. Appl Opt 1994;33:4497–500.
[69] Zuo C, Huang L, Zhang M, Chen Q, Asundi A. Temporal phase unwrapping algorithms for fringe projection profilometry: a comparative review. Opt Lasers Eng 2016;85:84–103.
[70] Wang T, Huang L, Zhu Y, Vescovi M, Khune D, Kang H, et al. Development of a position–velocity–time-modulated two-dimensional ion beam figuring system for synchrotron x-ray mirror fabrication. Appl Opt 2020;59:3306–14.
[71] Huang L, Wang T, Tayabaly K, Kuhne D, Xu W, Xu W, et al. Stitching interferometry for synchrotron mirror metrology at National Synchrotron Light Source II (NSLS-II). Opt Lasers Eng 2020;124:105795.